



# Polystyrene-templated hollow mesoporous magnetite as a bifunctional adsorbent for the removal of rhodamine B via simultaneous adsorption and degradation

Richky Wijaya Abadi<sup>a,1</sup>, Carlos Marcelino Setiawan<sup>a,1</sup>, Shella Permatasari Santoso<sup>a,b</sup>, Vania Bundjaja<sup>b</sup>, Artik Elisa Angkawijaya<sup>c</sup>, Yi-Fan Jiang<sup>d</sup>, Christian Julius Wijaya<sup>a,e</sup>, Suryadi Ismadji<sup>a,b</sup>, Ery Susiany Retnoningtyas<sup>a</sup>, Felycia Edi Soetaredjo<sup>a,b</sup>, Jindrayani Nyoo Putro<sup>a</sup>, Maria Yuliana<sup>a,\*</sup>

<sup>a</sup> Department of Chemical Engineering, Widya Mandala Surabaya Catholic University, Kalijudan 37, Surabaya 60114, Indonesia

<sup>b</sup> Department of Chemical Engineering, National Taiwan University of Science and Technology, 43, Keelung Rd., Section 4, Taipei 10607, Taiwan, ROC

<sup>c</sup> Graduate Institute of Applied Science and Technology, National Taiwan University of Science and Technology, 43 Keelung Road, Section 4, Taipei 10607, Taiwan, ROC

<sup>d</sup> Graduate Institute of Molecular and Comparative Pathobiology, School of Veterinary Medicine, National Taiwan University, Taipei, Taiwan, ROC

<sup>e</sup> Department of Chemical Engineering, Faculty of Industrial Technology and Systems Engineering, Institut Teknologi Sepuluh Nopember, Keputih Sukolilo, Surabaya 60111, Indonesia

## ARTICLE INFO

Editor: Apostolos Giannis

### Keywords:

Hollow mesoporous magnetite  
Bifunctional adsorbent  
Adsorption  
Catalytic degradation  
Rhodamine B

## ABSTRACT

Rhodamine B (RhB) is classified as one of the most hazardous pollutants due to its toxic and carcinogenic nature. This study uses a new class of adsorbent, polystyrene-templated hollow mesoporous magnetite (HMM), to remove RhB from the aqueous solution via simultaneous adsorption and degradation. The obtained HMM is spherical with a 320 – 350 nm particle size. The particle is integrated with a hollow core at ca. 230 nm in diameter. HMM possesses a porous interior, with the respective specific surface area and pore volume of 132.0 m<sup>2</sup>/g and 0.63 cm<sup>3</sup>/g. Its adsorption/desorption isotherm exhibits the typical type-IV IUPAC classification with the H4-type hysteresis profile, indicating the presence of mesoporous wedged-shaped pores. The influences of three independent variables on the RhB removal rate are studied, including pH, adsorbent loading  $m_c$ , and temperature  $T$ . The highest removal rate of RhB is obtained at 99.7% when pH = 6,  $m_c$  = 0.8 wt%,  $T$  = 50 °C, and time = 240 min. The study suggests that the whole removal process of RhB follows the pseudo-second-order law and multilayer mechanism and is generally favorable, spontaneous, and endothermic. Further elaboration using the multi-linear IPD shows that surface diffusion plays a major role in removing RhB. At the same time, the modified Langmuir also considers the Fenton degradation reaction as one of the factors that promote the dye removal, particularly in higher  $T$ . Based on the study, HMM exhibits excellent performance in removing RhB by facilitating both adsorption and Fenton reaction in a one-step process.

## 1. Introduction

Recently, water pollution caused by the textile industries has brought much attention. A study mentioned that around 17–20% of the industrial waste pollutant, e.g., synthetic dyes and heavy metals, originated from the coloring process of the textile industries [1]. Rhodamine B (RhB), one of the most commonly-used cationic dyes in textile industries [2], is known to have a dangerous effect on the environment and the

living creatures in the ecosystem [3]. Jain et al. (2007) reported that potable water contaminated with rhodamine dyes causes subcutaneous tissue-borne sarcoma; therefore, it is highly carcinogenic [4].

According to the Indonesian Ministry of Industry, the growth rate of the textile industries reached 15% in 2019, indicating a rapid engagement of this industrial sector in Indonesia [5]. Another report also claims that approximately 15% of the textile industries in Indonesia are not accommodated by the wastewater treatment plant [6]. These may

\* Corresponding author.

E-mail address: [mariayuliana@ukwms.ac.id](mailto:mariayuliana@ukwms.ac.id) (M. Yuliana).

<sup>1</sup> These authors contributed equally to this work.

undoubtedly raise various environmental problems, as releasing the untreated wastewater could endanger the environment and public health. Therefore, it is imperative to look for a suitable and facile technique to eliminate dyes from the wastewater before discharge.

Recent studies have reported several techniques to overcome the problems caused by textile industrial wastewater, namely ion exchange [7], chemical precipitation [8], and adsorption [9]. Among these techniques, adsorption shows better potential in wastewater treatment due to its simplicity, low operation cost, and insensitivity to toxic substances [10]. Previous studies have reported the use of various high-performance adsorbents to remove synthetic dyes, drugs, organic components, and heavy metals from the wastewater, i.e., biomaterials [1], modified clay minerals [11,12], activated carbon [13], metal oxides [14], metal-organic framework [15–17] and magnetite nanoparticles [18].

Of the various adsorbents available for wastewater treatment, magnetite nanoparticles attract much attention due to their (1) low toxicity [19], (2) high stability in various pH [20,21], (3) adequate surface area and pore volume to remove contaminants, (4) high catalytic activity in the Fenton degradation process to eliminate persistent pollutants [15,22], and (5) paramagnetic characteristics, which make them quickly recovered after use [23]. Magnetite nanoparticles are considered a suitable material for the removal of synthetic dyes, particularly Rhodamine B, as they can release the di- and trivalent of iron ions ( $\text{Fe}^{2+}$  and  $\text{Fe}^{3+}$ , respectively) in water, which act as the catalysts in the degradation of Rhodamine B by peroxides to produce less harmful components [24]. However, the microporous structure with a 0.7 nm average pore diameter [21] that the magnetite nanoparticles have, in contrast, makes their performance in the adsorption of RhB unsatisfactory. The diameter of RhB is reported to be two times larger than the pore diameter of magnetite nanoparticles (~1.44 nm) [25]; thus, RhB will be difficult to be adsorbed by the magnetite nanoparticles.

Various modification routes have been reported to improve the magnetite adsorptive ability on the synthetic dyes; mostly by combining the magnetite nanoparticles with other materials, e.g., MIL-53Fe/biochar [26], chitosan [27], chitosan/vanadium/titanium [28], activated carbon [29], cellulose aerogel [30], and cellulose/graphene oxide hydrogel [31]. However, these magnetite composites are complicated to prepare and may escalate the cost. In this study, we fabricate a new magnetite class, hollow mesoporous magnetite (HMM), by enlarging the pore diameter of magnetite and graft a hollow core. The hollow structure has been reported to increase the adsorbent performance in various pollutant removals, resulting from the higher accessibility of the hollow materials, given by their larger pore size [32,33]. A template-directed method is employed with polystyrene (PS) selected as the hard template to incorporate the hollow core in HMM. PS is preferred due to its facile surface functionalization [34] and uniformity in particle size [35]. Without adding other composite materials, this modification approach simplifies the fabrication method to obtain a bifunctional adsorbent that can facilitate adsorption and degradation.

To evaluate the performance of HMM, the influence of three important parameters, e.g., pH, temperature ( $T$ , °C), and adsorbent loading ( $m_c$ , wt%), will be investigated. Meanwhile, the adsorption behavior of the RhB onto HMM surface is assessed via kinetic, isotherm, and thermodynamic studies. The modified Langmuir equation will be used to represent the degradation phenomena, and the mineralization study will be further performed to verify the decomposition of RhB. The simulation of the RhB removal mechanism using HMM will be also employed, as it is important to investigate the feasibility and limitation of HMM from technological viewpoint.

## 2. Materials and methods

### 2.1. Materials

Styrene ( $\text{C}_6\text{H}_5\text{CHCH}_2$ , CAS No. 100–42–5,  $\geq 99.0\%$  purity),

methacrylic acid ( $\text{C}_4\text{H}_6\text{O}_2$ , CAS No. 79–41–4,  $\geq 99.0\%$  purity), ethylene Glycol ( $\text{C}_2\text{H}_6\text{O}_2$ , CAS No. 107–21–1,  $\geq 99.0\%$  purity), hexamethylenetetramine (HETM) ( $\text{C}_2\text{H}_{12}\text{N}_4$ , CAS No. 100–97–0,  $\geq 99.0\%$  purity), and RhB ( $\text{C}_{28}\text{H}_{31}\text{ClN}_2\text{O}_3$ , CAS No. 81–88–9,  $\geq 95.0\%$  purity) are obtained from Sigma-Aldrich (Germany), while potassium persulfate ( $\text{K}_2\text{S}_2\text{O}_8$ , CAS No. 7727–21–1,  $\geq 99.0\%$  purity), potassium nitrate ( $\text{KNO}_3$ , CAS No. 7757–79–1,  $\geq 99.0\%$  purity), and iron (II) chloride ( $\text{FeCl}_2 \cdot 4 \text{H}_2\text{O}$ , CAS No. 13478–10–9,  $\geq 99.0\%$  purity) are purchased from Supelco (Germany). All other reagents, e.g., sodium hydroxide (NaOH, CAS No. 1310–73–2,  $\geq 97.0\%$  purity), sulfuric acid ( $\text{H}_2\text{SO}_4$ , CAS No. 7664–93–9,  $\geq 98\%$  purity), and hydrogen peroxide ( $\text{H}_2\text{O}_2$ , CAS No. 7722–84–1, 35% purity) are supplied by Merck (Germany). All chemicals are of analytical grade and used as received.

### 2.2. Preparation of HMM

Fabrication of HMM using a template-directed method begins with the functionalization of the PS surface, following the method proposed by Huang and Tang (2005) [21] with some modifications. In a typical synthesis of functionalized PS, 18 ml of styrene, 2 ml of methacrylic acid, 0.2 g of potassium persulfate, and 160 ml of deionized water are introduced into a glass beaker and mixed for 24 h at 80 °C. The resulting colloidal solution is freeze-dried (–40 °C, 0.02 mbar) overnight to obtain the dried functionalized PS.

The fabrication of HMM continues by diluting 90 ml of ethylene glycol into 360 ml of deionized water. Then 0.6 g PS, 10.6 mmol of  $\text{FeCl}_2 \cdot 4 \text{H}_2\text{O}$ , 3.3 mmol of  $\text{KNO}_3$ , and 42.9 mmol of HETM are added to the water-ethylene glycol mixture. The solution is heated to 80 °C and continuously agitated at 800 rpm under sonication for 3 h. The generated PS-coated magnetite ( $\text{PS}@ \text{Fe}_3\text{O}_4$ ) particles are collected by centrifugation at 6000 rpm for 5 min and repeatedly washed with deionized water. The solid product is then dried at 60 °C to remove the excess water and subsequently calcined at 350 °C for 3 h to obtain HMM.

### 2.3. Characterization of HMM

HMM was characterized using scanning electron microscopy with energy dispersive X-Ray spectroscopy (SEM/EDX), nitrogen sorption, and X-Ray Powder Diffraction (XRD). The SEM images are obtained by SEM JEOL JSM-6500 F (Jeol Ltd., Japan) at 15 kV and 10.4–10.5 mm working distance. Meanwhile, TEM is conducted on JEOL JEM-2100 (Jeol Ltd., Japan) at 200 kV. The nitrogen sorption analysis is carried out using Micromeritics ASAP 2010 Sorption Analyzer at 77 K to obtain the textural properties of HMM. The sample is degassed at 473 K for two hours before analysis. The crystallinity profile of HMM is acquired on an X'PERT Analytical Pro X-Ray diffractometer (Philips-FEI, Netherlands). The respective running voltage, tube current, and monochromatic Cu  $\text{K}\alpha 1$  radiation are set at 40 kV, 30 mA, and 0.154 nm with  $2\theta = 20\text{--}70^\circ$ . The point-of-zero-charge ( $\text{pH}_{\text{pzc}}$ ) of HMM was measured using Malvern Zetasizer Nano Z (Malvern Panalytical Ltd., UK) with a pH range of 2–10.

### 2.4. The adsorption and degradation of RhB via Fenton reaction

#### 2.4.1. The influence of pH, temperature, and adsorbent loading

The adsorption experiments are initially carried out in a series of flasks at various pH (pH = 2, 4, 6, 8, 10) to obtain the optimum pH for RhB removal. One percent of HMM ( $m_c = 1.0 \text{ wt}\%$ ) is added to the RhB solution (initial RhB concentration = 50 mg/L) and continuously shaken in a water bath for 240 min at 30 °C. The equilibrium adsorption time ( $t_{\text{eq}}$ ) is determined using the procedures mentioned in Section 2.4.2. The pH where the highest RhB removal is observed is the optimum pH (pH-opt).

After obtaining pH-opt, various HMM loadings ( $m_c = 0.1\text{--}1.0 \text{ wt}\%$ ) and 5 wt% hydrogen peroxide (50% solution) are subjected to a 240-min adsorption process at pH-opt, constant temperature and agitation speed

(250 rpm). Three adsorption temperatures ( $T = 30, 40, 50\text{ }^{\circ}\text{C}$ ) are employed to study the temperature influence on the removal of RhB. The concentration of RhB in the supernatant is measured using Shimadzu UV-Vis spectrophotometer 2600 (Shimadzu, Japan) at a wavelength of 553 nm. All experimental batches in this section are run in triplicates.

#### 2.4.2. Kinetic, isotherm, and thermodynamic studies

The adsorption kinetics is used to determine the equilibrium time ( $t_{eq}$ ) for the adsorption of RhB onto HMM. It is conducted at pH-opt,  $m_c = 0.8\text{ wt}\%$  and various temperatures ( $T = 30, 40, 50\text{ }^{\circ}\text{C}$ ). Each beaker glass is collected at different time intervals to measure the loaded amount of RhB in HMM. The isotherm and thermodynamic studies are further performed by adding various HMM loading ( $m_c = 0.1, 0.2, 0.3, 0.4, 0.5, 0.6, 0.7, 0.8, 0.9, 1.0\text{ wt}\%$ ) to the RhB solution at three temperature levels ( $T = 30, 40, 50\text{ }^{\circ}\text{C}$ ). The adsorption time is set at  $t_{eq}$ . All runs in this section are employed by adding 5 wt% hydrogen peroxide (50% solution) at the beginning of the adsorption and conducted in triplicates to increase the confidence level of the data.

The adsorption capacity at a specific time ( $Q_t$ ) and at equilibrium ( $Q_e$ ) can be calculated using Eqs. (1) and (2), where  $C_0$ ,  $C_t$ , and  $C_e$  represent the initial RhB concentration, the RhB concentration at time  $t$  and the equilibrium concentration of RhB in the solution (mg/L),  $w_c$  corresponds to the loaded mass of HMM (g), and  $V$  equals to the volume of RhB solution.

$$Q_t = \frac{(C_0 - C_t)V}{w_c} \quad (1)$$

$$Q_e = \frac{(C_0 - C_e)V}{w_c} \quad (2)$$

The equilibrium data are then fitted to (1) Langmuir, Freundlich, Temkin, liquid-phase BET isotherms, and (2) modified Langmuir approach to elaborate the RhB adsorption and degradation behaviors. The obtained isotherm parameters are further analyzed to determine Gibbs free energy ( $\Delta G^{\circ}$ ), enthalpy ( $\Delta H^{\circ}$ ), and entropy ( $\Delta S^{\circ}$ ).

#### 2.4.3. Mineralization study

The mineralization of RhB is verified by the total organic carbon (TOC) analysis by varying the contact time ( $t = 0 - 240\text{ min}$ ) between RhB solution (50 mg/L) and HMM under optimum conditions. The TOC analysis is performed using Mettler Toledo 6000TOCi (Mettler Toledo, USA), and the mineralization rate ( $M$ ) is computed by the Eq. (3), where  $\text{TOC}_0$  corresponds to the initial TOC of the RhB solution, and  $\text{TOC}_t$  refers to the TOC of the RhB solution at time  $t$ .

$$M(\%) = \frac{(\text{TOC}_0 - \text{TOC}_t)}{\text{TOC}_0} \times 100 \quad (3)$$

### 3. Results and discussions

#### 3.1. The mechanism scheme of HMM fabrication

Fig. 1 depicts the synthesis route of HMM: (1) firstly, PS nanospheres

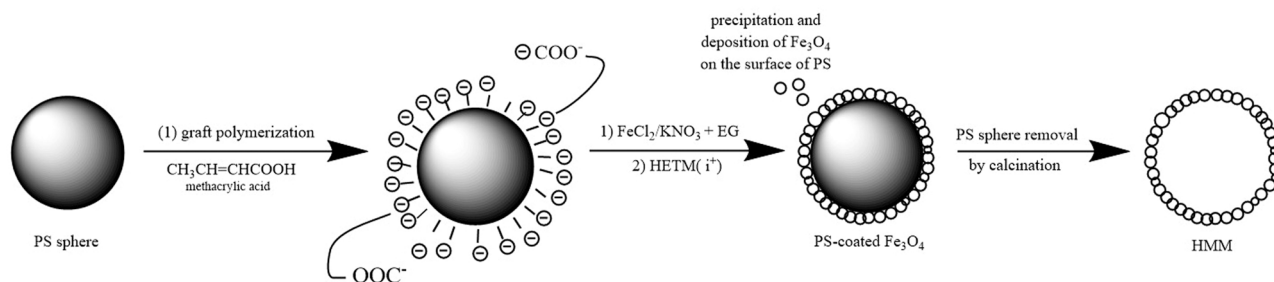


Fig. 1. The schematic mechanism of the HMM fabrication.

are simultaneously prepared and functionalized with carboxyl group via graft polymerization of methacrylic acid; (2) in a dispersion system containing negatively charged PS templates and ethylene glycol/water system, the Ferro chloride interlinks with the surface of carboxyl-functionalized PS and undergoes the precipitation reaction with  $\text{KNO}_3$  and HETM to form magnetite-coated PS spheres; (3) PS, as the rigid template of the core, and the other organic impurities are then removed by calcination, to obtain the HMM particles.

#### 3.2. Material characterizations

Fig. 2a shows the SEM image of the nano spherical PS template, while Fig. 2b–g present the SEM and TEM images of the HMM at various magnifications. The template is spherical with a uniform size at ca. 150–180 nm (Fig. 2a). Notably, the HMM nanoparticle has a sphere-like morphology with an integrated hollow core (Fig. 2b–g), indicating that the PS template has been completely decomposed during the calcination process. The particle size of HMM is estimated at ca. 320–350 nm, and its integrated hollow-core size is 230 nm. The thickness of the shell is calculated in the range of 45–60 nm.

The elemental mapping (Fig. 3a–e) demonstrates that the iron, oxygen, carbon, nitrogen, and zirconium elements are distributed throughout the HMM particles with the respective atomic composition of 39.6%, 52.1%, 5.09%, 1.64%, and 1.59% (Fig. 3 f). The EDX result exhibits two strong peaks assigned to the iron and oxygen elements, indicating the plentiful presence of  $\text{Fe}_3\text{O}_4$  in the HMM particles [34]. Meanwhile, nitrogen and zirconium elements are impurities retained from the fabrication and analysis procedures.

Six characteristic peaks are detected for both magnetite and HMM at  $2\theta = 30.4^{\circ}, 35.8^{\circ}, 43.5^{\circ}, 53.8^{\circ}, 57.4^{\circ}, 63.1^{\circ}$ , and  $30.0^{\circ}, 35.1^{\circ}, 42.8^{\circ}, 53.2^{\circ}, 56.7^{\circ}, 62.2^{\circ}$ , respectively (Fig. 4a). The result indicates that magnetite and HMM nanoparticles possess similar crystal structures. Using the Scherrer equation, the estimated crystal size of the magnetite particles in HMMs is 2.89 nm, indicating that the constituting magnetite is in the nanoparticle size range [36].

The textural properties of HMM are determined by nitrogen sorption and are presented in Fig. 4b. The nitrogen adsorption/desorption isotherm of HMM exhibits a typical type-IV isotherm with the hysteresis profile of H4, indicating the presence of a mesoporous structure with wedged-shaped pores [37]. The BJH isotherm describes the pore size distribution of the particles and detects one dominant peak at 37.8 nm (Fig. 4b (inset)), which is in the mesoporous range. The significant increase of the nitrogen adsorbed at  $p/p^0$  close to unity also suggests the presence of the macroporous structure within the particle, corresponding to the integrated hollow core. The adsorption and desorption profiles, which are almost attached, also imply that the pores are highly accessible. The specific surface area and pore volume of HMM obtained in this study are  $132.0\text{ m}^2/\text{g}$  and  $0.63\text{ cm}^3/\text{g}$ , higher by 1.4 and 10.5 folds, respectively, compared to a similar study of HMM [21]. The  $\text{pH}_{\text{pzc}}$  of HMM is obtained at  $\text{pH} = 8.4$  (Fig. 4c). At  $\text{pH}$  lower than  $\text{pH}_{\text{pzc}}$ , HMM protonates to form  $\text{FeOH}_2^+$  due to excess hydronium ( $\text{H}^+$ ) ions in the solution. Meanwhile, HMM is deprotonated at  $\text{pH} > \text{pH}_{\text{pzc}}$  and converts

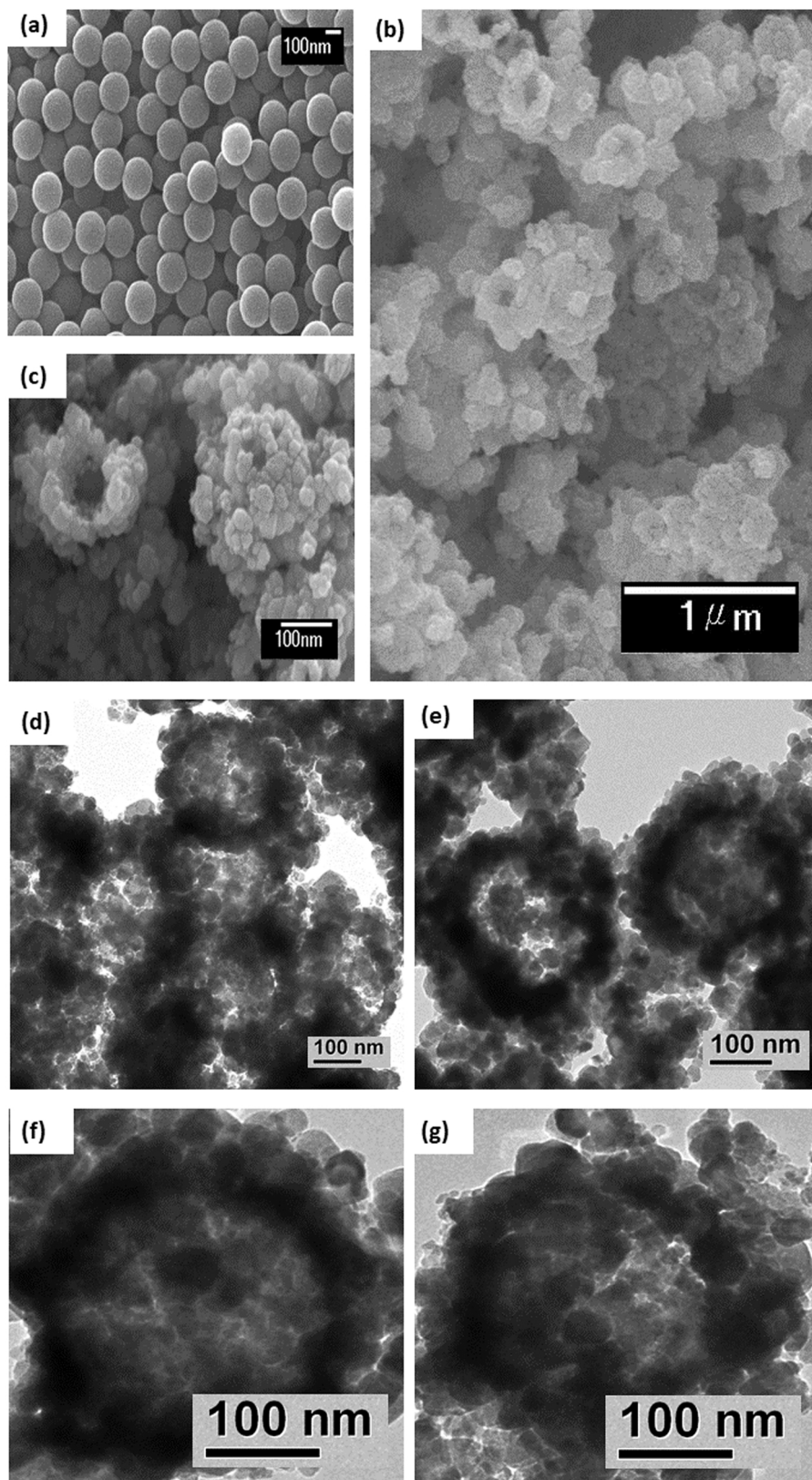


Fig. 2. (a) SEM image of nano spherical PS template, (b-c) SEM, and (d-g) TEM images of HMM at various magnifications.

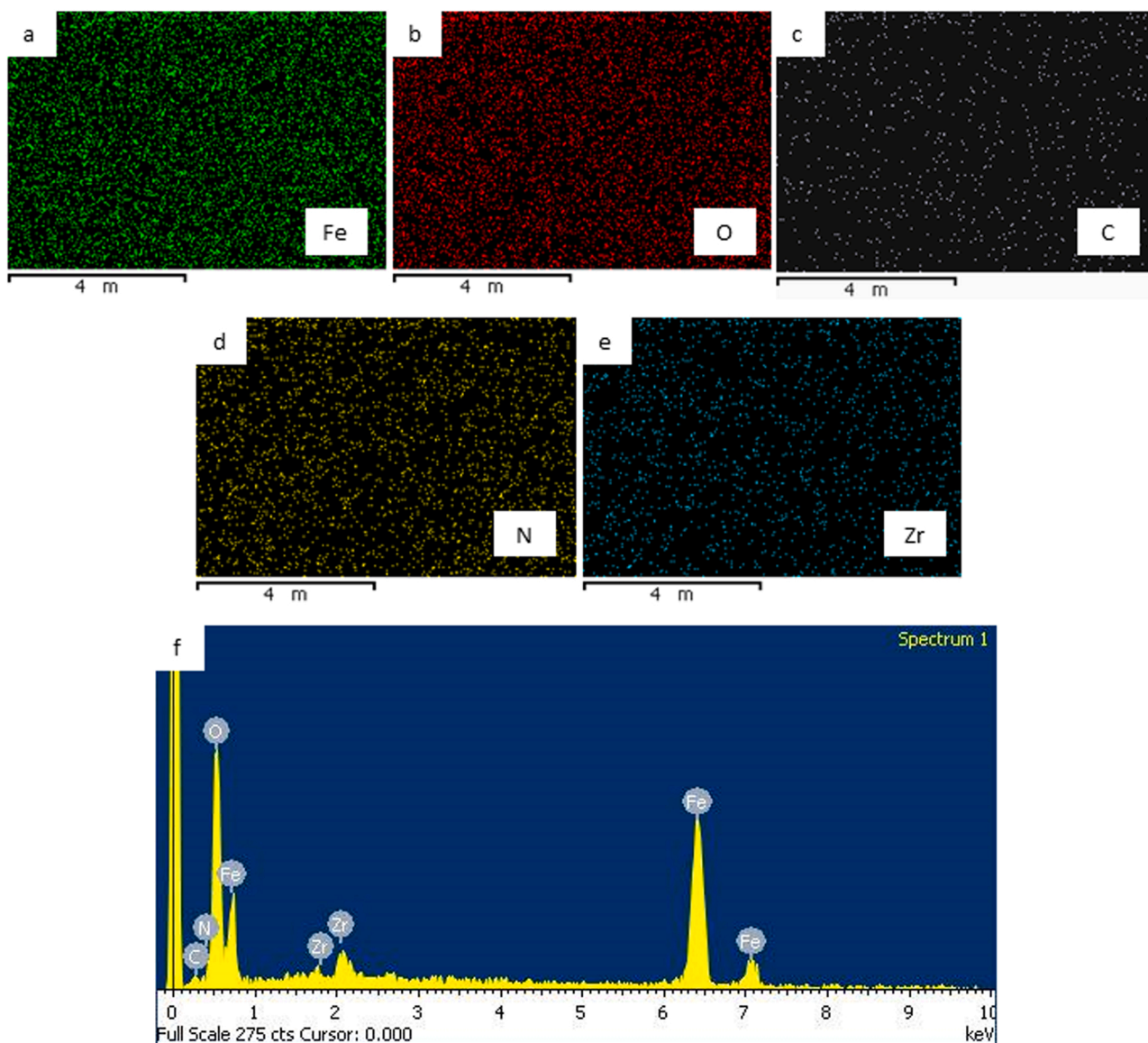


Fig. 3. (a) – (e) The elemental mapping and (f) EDX spectrum of HMM.

its active side to the negatively charged  $\text{FeO}^-$ .

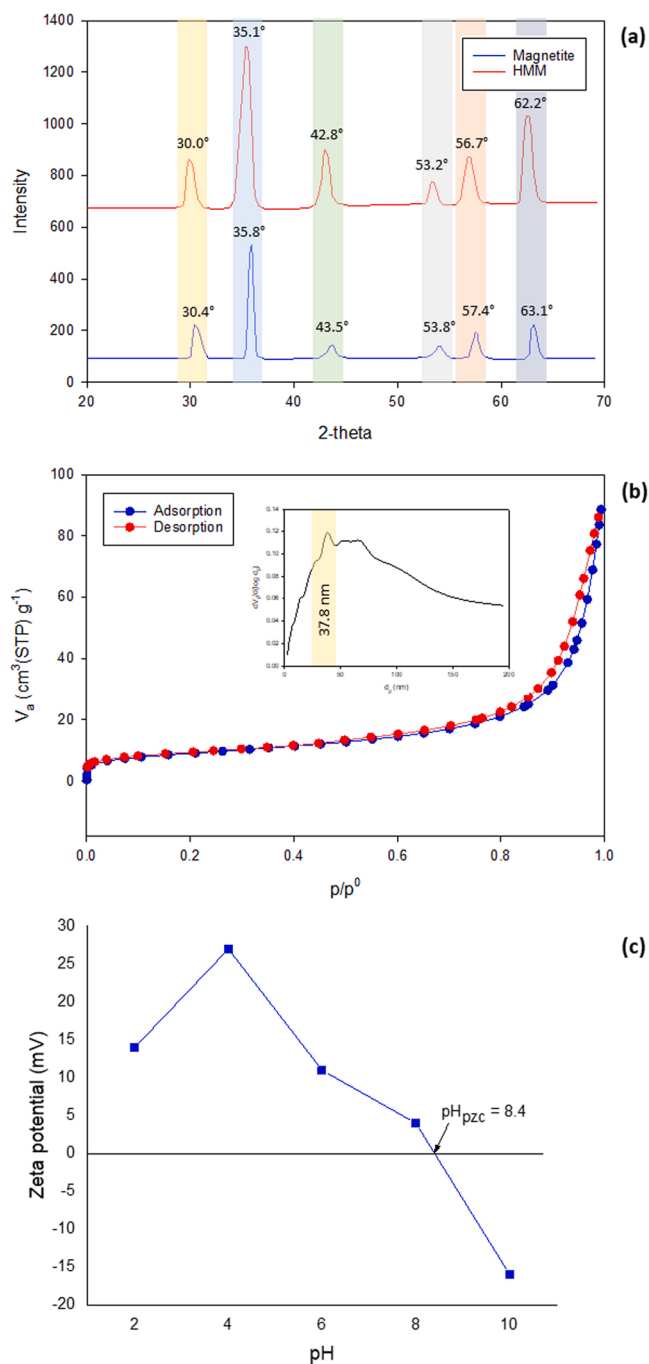
### 3.3. Influence of pH, temperature, and adsorbent loading on the RhB removal using HMM

The pH solution plays an essential role in the adsorption and degradation processes because, in most cases, the surface charge of the adsorbent, the adsorbate ion form, and the electrostatic interaction between the two change along with the pH level. Fig. 5 shows that the removal rate of RhB via adsorption by HMM increases from 49.8% to 71.1% as the pH escalates from pH = 2 to pH = 6 and subsequently decreases to 31.8% as the pH rises to pH = 10. The results indicate that the removal of RhB is limited to a pH lower than  $\text{pH}_{\text{pzc}}$  (8.4), with the maximum removal at pH = 6. Kerkez et al. (2014) studied that RhB exists in 3 ionic states, e.g., zwitterionic ( $\text{RhB}^{\pm}$ ) and two cationic forms ( $\text{RhBH}^+$  and  $\text{RhBH}^{2+}$ ), depending on the pH level of the solution [38]. Moreover, Hou et al. (2011) also reported that the  $\text{pH}_{\text{pzc}}$  of RhB is found at 4.1 – implying that RhB is positively charged below its  $\text{pH}_{\text{pzc}}$  and negatively charged as the pH increase [39]. The low removal of RhB at pH = 2 can be attributed mainly to the electrostatic repulsion between the cationic RhB ions ( $\text{RhBH}^+$  and  $\text{RhBH}^{2+}$ ) and  $\text{FeOH}_2^+$  ions from HMM.

At higher pH, the ionic transition of RhB from the cationic to zwitterionic form ( $\text{RhB}^{\pm}$ ) induces its electrostatic interaction with the positively charged HMM, increasing the removal rate of RhB. However, at pH > 6, the repulsion between the zwitterionic RhB ( $\text{RhB}^{\pm}$ ) and deprotonated HMM ( $\text{FeO}^-$ ) occurs and causes the reduction of RhB removal.

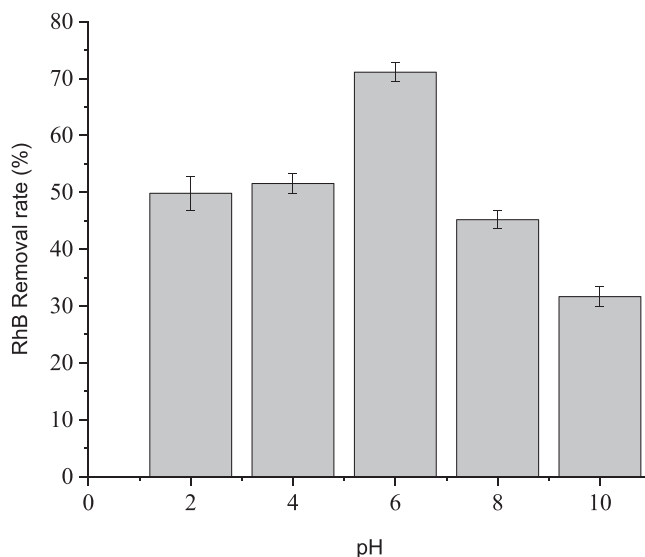
At pH-opt (pH = 6), the RhB removal at various  $T$  and  $m_c$  are summarized in Fig. 6. The highest reduction of RhB using HMM (99.7%) is achieved at  $T = 50^\circ\text{C}$  and  $m_c = 0.8$  wt%. The experimental results show a significant increase in the removal of RhB when the temperature is elevated from  $30^\circ\text{C}$  to  $50^\circ\text{C}$  within all tested  $m_c$ . It can be contributed by the higher mobility and kinetic energy that the HMM and RhB molecules have at higher  $T$ . This intensifies the collision between both adsorbent and adsorbate, induces easier attainment of the activation energy, and subsequently results in a higher removal rate [40]. Chowdhury et al. (2011) added that the correlation between the mass transfer rate of the adsorbate and temperature is straightforward and proportional [41].

Fig. 6 also depicts that the HMM loading ( $m_c$ ) remarkably influences the removal rate of RhB, particularly in the first eight points (at  $m_c = 0.1 - 0.8$  wt%). The increasing removal rate of RhB, along with the adsorbent loading, indicates that the available surface area of the adsorbate



**Fig. 4.** (a) XRD diffraction of magnetite and HMM, (b)  $N_2$  adsorption and desorption isotherms with its corresponding BJH pore size distribution curve (inset) of HMM, (c)  $pH_{pzc}$  of HMM.

contributes proportionally to the RhB adsorption and degradation rate [42]. However, at higher  $m_c$ , we see a slight decrease in the removal rate of RhB. A high concentration of adsorbent in the solution narrows the distance between the adsorbent particles and leads the particle to stack and aggregate with each other. This interparticle movement decreases the available surface area for adsorption and degradation, reducing the HMM performance in the RhB removal. Another reason is probably caused by the excess of  $Fe^{3+}$  and  $Fe^{2+}$  ions in the solution. Prasetyo et al. (2019) reported that a proportional amount of  $Fe^{3+}$  and  $Fe^{2+}$  ions are required to generate hydroxyl and hydroperoxyl radicals in order to degrade organic contaminants [43]; an excess of these two ions, on the contrary, will lead to the recombination reaction of the radicals, which



**Fig. 5.** The influence of pH on the adsorption of RhB.

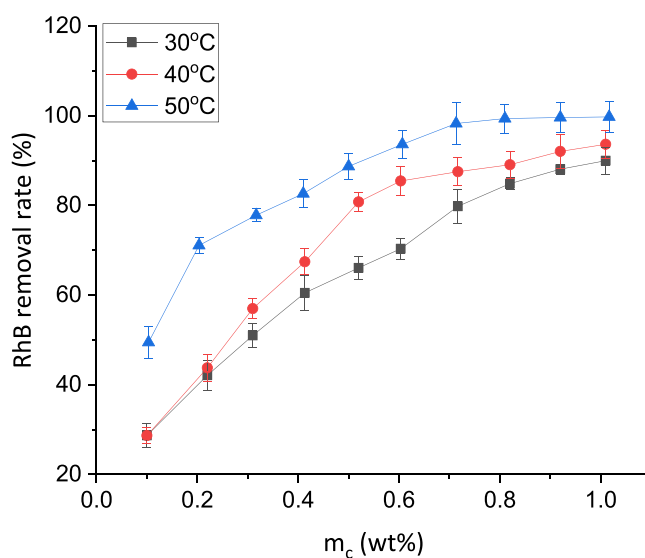


**Fig. 6.** The influence of temperature (T) and HMM loading ( $m_c$ ) on the removal of RhB at pH = 6.

hinders the degradation process [35].

A comparison of the RhB removal rate using HMM with other existing catalysts is given in Table 1. Notably, the initial concentration of dye ( $C_0$ ) significantly influences the dye removal rate, from  $> 95\%$  at  $C_0 = 10$  mg/L to  $\sim 70\%$  at  $C_0 = 100$  mg/L. The performance comparison between the non-hollow  $Fe_3O_4$  and HMM in this study also shows that integrating a hollow structure significantly increases the removal rate of RhB, as it enhances the accessibility of the material for the dye molecules to diffuse towards the interior part of HMM. Moreover, among the studies on removing RhB via simultaneous adsorption and degradation, HMM shows a higher activity compared with the other materials reported by Hu et al. (2015) and Navarathna et al. (2019) [26,45]. This shows that HMM, as a bifunctional adsorbent, can enhance the removal rate of RhB at a comparable operating condition.

### 3.4. Kinetic study

Several data at a various time is fitted into three kinetic models, i.e., pseudo-first-order, pseudo-second-order, and intraparticle diffusion

**Table 1**

The comparison of RhB removal activity of various adsorbents.

Material	Adsorption system/mechanism	Operating condition	Dye removal rate (%)	Reference
SDS-modified laterite soil	Batch, adsorption	pH = 4, $t = 60$ min, $T = 25$ °C, $m_c = 2.5$ wt%, dye initial concentration = $10^{-5}$ M	98.85%	[12]
Magnetite	Batch, Fenton degradation via electrolysis	pH = 3, $t = 180$ min, $m_c = 10$ ppm, dye initial concentration = 10 mg/L, voltage = 8 V	97.3%	[44]
Ag@AgBr/SBA-15	Batch, adsorption and photocatalytic degradation	pH = 4.28, $T = 20$ °C, $m_c = 0.03$ wt%, dye initial concentration = 20 mg/L	88%	[45]
Hierarchical UiO-66	Batch, adsorption	pH = 5, $t = 2$ h, $T = 30$ °C, dye initial concentration = 38 mg/L	85%	[16]
MIL-53 Fe/magnetite/biochar	Batch, adsorption and photocatalytic degradation	pH = 6, $t = 20$ h, $T = 25$ °C, dye initial concentration = 50 mg/L	70%	[26]
Magnetic hollow mesoporous silica	Batch, adsorption	pH = 7, $t = 30$ s, $T = 25$ °C, $m_c = 0.1$ wt%, dye initial concentration = 100 mg/L	79%	[46]
UiO-66-(COOH) <sub>2</sub>	Batch, adsorption	pH = 7, $t = 12$ h, $T = 30$ °C, dye initial concentration = 3000 mg/L	N/A ( $Q_e = 2200$ mg/g)	[47]
Non-hollow Fe <sub>3</sub> O <sub>4</sub>	Batch, adsorption and Fenton degradation	pH = 6, $t = 240$ min, $T = 50$ °C, $m_c = 0.8$ wt%, dye initial concentration = 50 mg/L	89.8%	This study
HMM	Batch, adsorption and Fenton degradation	pH = 6, $t = 240$ min, $T = 50$ °C, $m_c = 0.8$ wt%, dye initial concentration = 50 mg/L	99.7%	This study

(IPD), as seen in Fig. 7. The kinetic study shows that the capacity of HMM increases significantly in the first thirty minutes and slows down after that until it reaches the equilibrium at 240 min. A similar trend is observed for all tested  $T$ , with the difference only in the adsorption and degradation capacity at equilibrium. Elevating the temperature from 30 °C to 50 °C promotes a higher removal rate of RhB and stronger HMM capacity from 51.7% and 2.43 mg/g to 98.4% and 4.25 mg/g, respectively. This could be attributed to the greater diffusion ability of RhB molecules to the active sites on the surface of adsorbent at higher  $T$ . Chowdhury et al. (2011) also reveal that increasing temperature escalates the mass transfer diffusion rate as the mobility of both adsorbate and adsorbent particles enhances, intensifying the collision between them [41].

Meanwhile, Jiang et al. (2018) mentioned that increasing the adsorption system temperature lowers the intramolecular energies, facilitating easier interaction between RhB and HMM [48]. The degradation of RhB due to the Fenton reaction is also controlled by the temperature. Increasing the temperature causes the formation of hydroxyl radical ( $\bullet$ OH) and hydroperoxyl radical ( $\bullet$ OOH) ions. The attack of  $\bullet$ OH and  $\bullet$ OOH in the bulk solution induces the fragmentation of the RhB aromatic chain into carbon dioxide and water [49].

The fitted parameters of the three kinetic models are summarized in Table 2. Based on the value of  $R^2$ , it is suggested that the pseudo-second-order kinetic model represents the experimental data better than the other two. The calculated  $Q_e$  values are also consistent with the experimental results, which conclude the better fit of RhB adsorption on HMM to the pseudo-second-order model. This result indicates that the removal of RhB tends to be chemically controlled, as it involves both degradation and adsorption of RhB onto the active sites of HMM surface.

The lower values of kinetic constants ( $k_1$  and  $k_2$ ) are also observed when the temperature is enhanced from 30 °C to 50 °C. At higher  $T$ , the faster kinetic mobility of RhB and HMM molecules due to the lower viscosity of the RhB solution causes RhB to migrate from the solid phase (HMM surface) to the bulk solution due to excessive collision between the two, hence, decreasing the removal rate of RhB [50]. Moreover, while at some point, more  $\bullet$ OH and  $\bullet$ OOH radicals at higher  $T$  are desirable to promote the degradation of RhB, the excess amount of these two in the system may cause a competitive reaction between RhB and H<sub>2</sub>O<sub>2</sub> with the radical ions, and consequently lower the sorption rates [51].

The multi-linear IPD (Fig. 7c) is used to elaborate the mechanism of the RhB removal, where the fitted data at all temperatures can be divided into three steps: (1) the film diffusion, where RhB penetrates to the external surface of HMM, (2) the intra-particle diffusion of RhB to the interior of HMM, and (3) the physical and chemical interaction between RhB and HMM molecules. Two interactions are probably involved

in the last step, including (1) the mesoporous filling mechanism with the presence of IPD forces via the electrostatic interaction between RhB and the active site of the HMM and (2) the Fenton (degradation) reaction [52,53]. Table 2 also shows that the adsorption constant ( $k_p$ ) in the IPD model differs for every step, where  $k_p$  in the first step ( $k_{p1}$ ) is higher than those of the second ( $k_{p2}$ ) and third ( $k_{p3}$ ) steps, implying that the most dominant step in this process is the adsorbate diffusion to the boundary layer of HMM, followed by the intra-particle diffusion and the adsorbate/adsorbent interaction.

### 3.5. Isotherm study

The equilibrium data at the three different temperatures are fitted into five types of adsorption isotherm model, e.g., Langmuir, Freundlich, Temkin, liquid-phase Brunauer-Emmet-Teller (BET), and modified Langmuir, with the tabulated isotherm parameters summarized in Table 3. Fig. 8 also depicts the fitted isotherms on the adsorption equilibrium data at  $T = 30$  °C using the first four isotherm models. Based on the Giles' classification, the adsorption of RhB (Fig. 8) exhibits an L-type sorption isotherm at low RhB concentration and an S-type sorption isotherm at moderate to the high content of RhB in an aqueous solution [54]. Type L suggests that the RhB molecules are adsorbed parallel to the surface, and there is no strong competition between the adsorbate and the solvent to occupy the binding site in HMM [55]. Meanwhile, the S-class observed at a higher concentration of RhB indicates cooperative adsorption [56], where the adsorbed RhB molecules interact strongly with the new adsorbate molecules, creating multilayer behavior of adsorption [57].

The above quasi-qualitative analysis is supported by the parameters seen in Table 3. Indicated by its higher  $R^2$  value, the Freundlich isotherm model describes the equilibrium data better than Langmuir and Temkin. The Freundlich model assumes that the adsorbent has a heterogeneous surface and different adsorption potentials [58]. It also suggests the multilayer adsorption of RhB on the surface of HMM [59]. This multilayer mechanism is also supported by the liquid-phase BET model, which gives the highest  $R^2$  (0.9108 – 0.9921) among the other models. Supporting the previous statement, the value of  $n$  (the maximum adsorption layers) obtained from the model also suggests that there are 2 – 3 layers of adsorbate on the solid surface of the adsorbent. The maximum adsorption capacity on the first layer ( $Q_{m(BET)}$ ) is found to be in the range of 3.99 – 8.11 mg/g according to the liquid-phase BET model, while Langmuir isotherm reveals that the  $Q_{m(L)}$  ranges from 23.9 to 37.4 mg/g.

As the  $1/n$  values at all  $T$  are lower than unity (0.39 – 0.65), the adsorption of RhB is considered a favorable process. Meanwhile, the increasing Freundlich constant ( $K_F$ ) with the temperature represents the

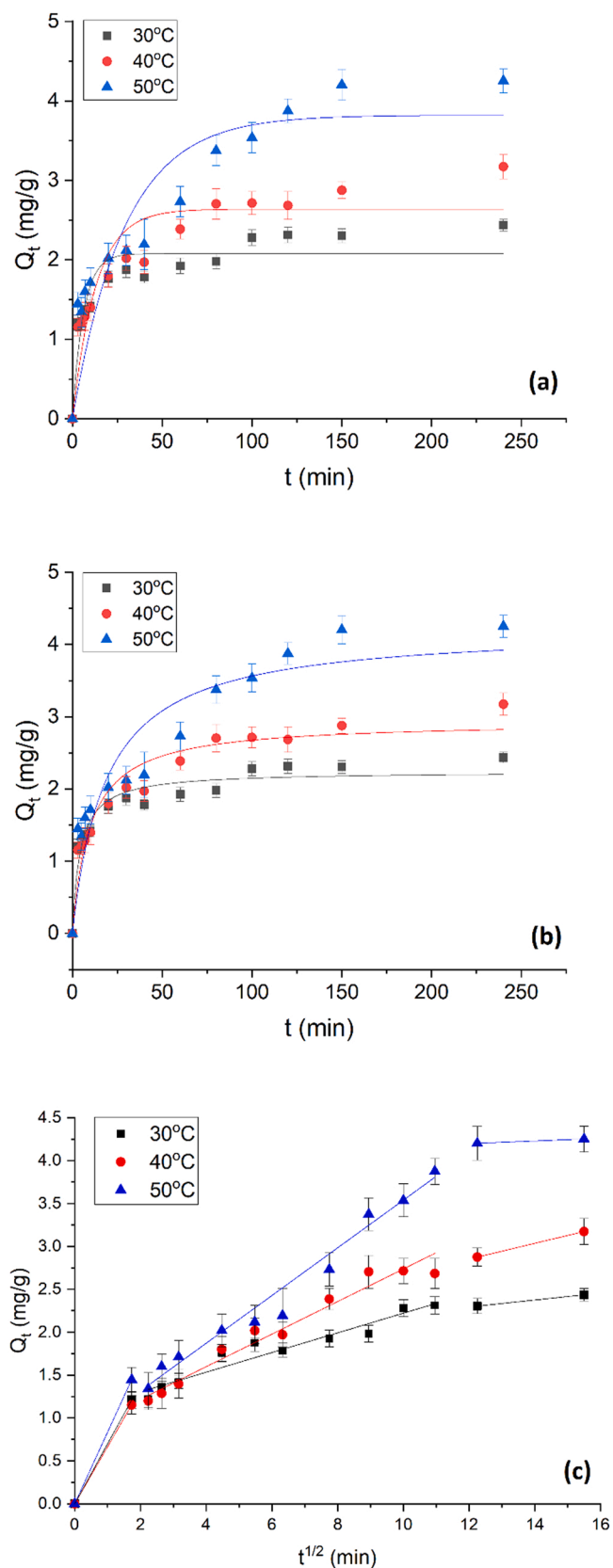


Fig. 7. The kinetic modeling of the adsorption and degradation of RhB using HMM: (a) pseudo-first-order; (b) pseudo-second-order; (c) intraparticle diffusion (IPD) model.

Table 2

The kinetic parameters of the adsorption and degradation of RhB using HMM at various temperatures (pH = 6,  $m_c = 0.8$  wt%, time = 240 min).

Parameters	Temperature (K)		
	303	313	323
$Q_{e=exp}$ (mg/g)	2.07	3.17	4.25
<i>Pseudo-first order</i>			
$Q_e$ (mg/g)	2.08	2.64	3.82
$k_1$ (g/mg.min)	0.16	0.08	0.03
$R^2$	0.8537	0.8439	0.7856
<i>Pseudo-second order</i>			
$Q_e$ (mg/g)	2.24	2.94	4.22
$k_2$ (g/mg.min)	0.10	0.04	0.01
$R^2$	0.9313	0.9291	0.8651
<i>Intraparticle diffusion (IPD)</i>			
$k_p$ (mg/g.min <sup>1/2</sup> )	0.124	0.183	0.267
1. $kp_1$	0.66	0.57	0.59
1. $kp_2$	0.28	0.18	0.11
1. $kp_3$	0.02	0.09	0.04
C	0.90	0.76	0.72
$R^2$	0.7689	0.8940	0.9380

Table 3

The fitted isotherm parameters for the adsorption and degradation of RhB.

Isotherm	Parameter	Unit	Temperature, K		
			303	313	323
Langmuir	$Q_{m(L)}$	mg/g	23.9	33.6	37.4
	$K_L$	L/mg	0.03	0.06	0.12
	$R^2$	–	0.7366	0.7936	0.8172
Freundlich	$K_F$	(mg/g)(L/mg) <sup>1/n</sup>	1.15	2.63	5.46
	1/n	–	0.65	0.42	0.39
	$R^2$	–	0.8122	0.8882	0.8039
Temkin	$K_T$	L/g	0.53	1.20	26.4
	$E_T$	J/mol	3.45	2.98	2.38
	$R^2$	–	0.6800	0.8450	0.6190
BET	$Q_{m(BET)}$	mg/g	3.99	5.76	8.11
	N	–	2.6	2.5	2.6
	$K_S$	L/mg	8.63	8.13	7.97
	$K_{L(BET)}$	L/mg	0.02	0.03	0.03
	$R^2$	–	0.9921	0.9511	0.9108
Modified Langmuir	$Q_m^*$	mg/g	23.9	30.7	37.4
	Q	kJ/mol	0.06	8.06	13.3
	$\Delta H$	kJ/mol	64.8	7.05	8.88
	$\theta_{ads}$	–	0.766	0.457	0.388
	$\theta_{deg}$	–	0.234	0.543	0.612
	$R^2$	–	0.7659	0.8375	0.6388

favorability of the RhB adsorption at the higher  $T$ . Both Langmuir ( $K_L$ ) and Temkin ( $K_T$ ) constants, as well as  $Q_{m(L)}$  and  $Q_{m(BET)}$ , also increase from  $T = 30^\circ\text{C}$  to  $T = 50^\circ\text{C}$ , which implies the endothermic nature of the adsorption of RhB.

The adsorption behaviors on the first layer and the upper layers are further observed using the adsorption equilibrium constant for the first layer ( $K_S$ ) and the upper layer ( $K_{L(BET)}$ ) obtained from the liquid-phase BET model. Table 3 shows that  $K_S$  decreases from 8.63 L/mg to 7.97 L/mg along with the temperature, indicating that the exothermic Fenton reaction happens on this very first layer of HMM. Meanwhile,  $K_{L(BET)}$  is escalating from 0.02 L/mg to 0.03 L/mg with the increasing temperature, which explains the occurring endothermic adsorption on the upper layers of HMM. The value of the heat of sorption ( $E_T$ ) obtained from the Temkin regression is monitored between 2.38 and 3.45 J/mol at the three temperature levels, indicating the adsorption step happens due to physical interaction – this result is in agreement with the previous kinetic study.

In this study, the modified Langmuir isotherm is also employed to study the distribution of active sites of HMM in the adsorption and degradation steps and elaborate on the behavior of the simultaneous adsorption and degradation process. This model assumes that the

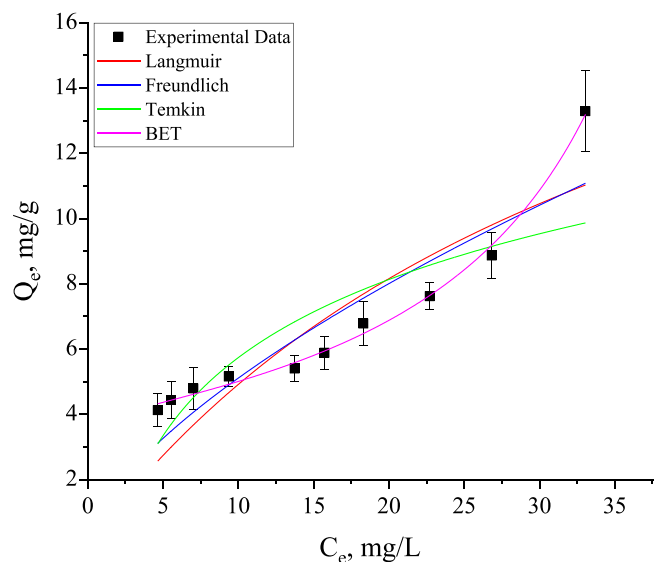


Fig. 8. The isotherm profile for the equilibrium data of RhB removal using HMM.

simultaneous adsorption and degradation process will result in a higher removal capacity than the typical adsorption because the total affinity between adsorbate and adsorbent is caused by two phenomena, e.g., chemical reaction and physical adsorption [60]. Laysandra et al. (2017) also find that the adsorption energy depends on two parameters: (1) the isosteric heat of adsorption ( $Q$ ) and (2) the heat of chemical reaction ( $\Delta H$ ). They also suggest that the active site on the adsorbent surface consists of two fractions: (1) the active site for adsorption (symbolized as  $\theta_{ads}$ ) and (2) the active site for degradation ( $\theta_{deg}$ ) [60]. The fitted equilibrium data to the modified Langmuir and its calculated parameters are presented in Fig. 9 and Table 3, respectively.

Similar values of the maximum adsorption capacity,  $Q_m^*$ , to the previous  $Q_{m(L)}$  (Table 3) are observed in all tested  $T$  with a proportional correlation between  $Q_m^*$  and  $T$ . This result shows that the ability of HMM to adsorb and degrade RhB is significantly influenced by  $T$ . The positive values of  $Q$  and  $\Delta H$  means that this process is endothermic [41]. At  $T = 30^\circ\text{C}$ , the respective  $\theta_{ads}$  and  $\theta_{deg}$  values are 76.6% and 23.4%, showing the dominance of adsorption in removing RhB from the

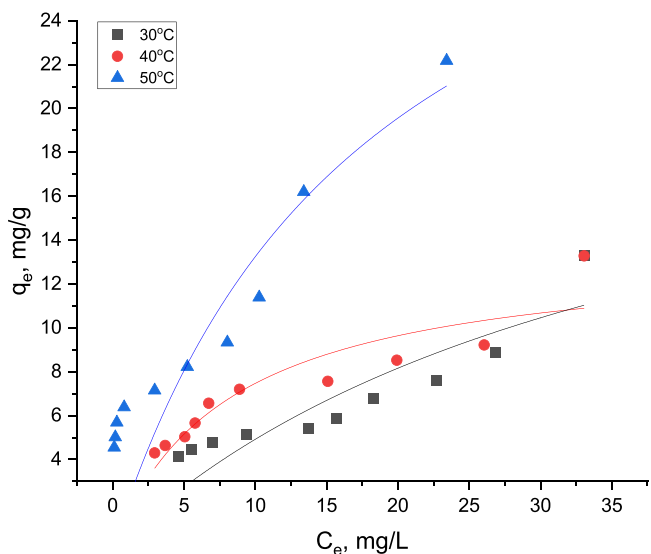


Fig. 9. The fitted equilibrium data of the simultaneous adsorption and degradation of RhB to the modified Langmuir model.

solution. However, it is observed that  $\theta_{deg}$  continues to escalate with the increasing temperature, reaching 61.2% at  $T = 50^\circ\text{C}$ . This result signifies that the amount of degraded RhB molecules enhances significantly compared to those in lower temperatures. Wan et al. (2015) reported that the number of hydroxyl and hydroperoxyl radicals formed from the decomposition of  $\text{H}_2\text{O}_2$  escalates at higher  $T$  due to the increase in the molecular kinetic energy, which then induces the rapid degradation of RhB [51].

### 3.6. Thermodynamic study

Table 4 summarizes the three important thermodynamic parameters, including Gibbs free energy change ( $\Delta G^\circ$ ), enthalpy ( $\Delta H^\circ$ ), and entropy ( $\Delta S^\circ$ ). The negative value of  $\Delta G^\circ$  at all tested  $T$  refers to the spontaneous and favorable removal of RhB using HMM. The decreasing value of  $\Delta G^\circ$  with the increase in  $T$  confirms the feasibility of RhB removal from the adsorption viewpoint. It also suggests that RhB has a stronger affinity on the surface of HMM at a higher  $T$ . Meanwhile, the positive  $\Delta H^\circ$  value (108.7 kJ/mol) confirms the endothermic behavior of the process. The high value of  $\Delta H^\circ$  ( $> 80$  kJ/mol) shows that the removal of RhB is dominantly governed by the chemical reaction [61], particularly at a high level of  $T$ . The  $\Delta S^\circ$  is observed at  $-357.3$  J/mol.K, indicating the decrease in disorder and randomness of adsorbate molecules distribution on the active sites due to the association between RhB and HMM [41].

### 3.7. Mineralization of RhB

Fig. 10 presents the profiles of the mineralization rate of RhB and the TOC content in the solution at various adsorption and degradation time. The two profiles show that the TOC content decreases significantly in the first 20 min, reaches a plateau zone in the middle, and steadily reduces the TOC during the remaining time. This pattern indicates that rapid mineralization of RhB to gaseous  $\text{CO}_2$  happens almost immediately during the first step. This is supported by the presence of vigorous bubbles observed after the addition HMM to the RhB solution during the experimental runs. A stagnant mineralization rate is then monitored from  $t = 20$  min to  $t = 60$  min, which implies that some dye molecules are decomposed to the lower molecular weight components [62], and these intermediates still contribute to the TOC content. The gradual increase of mineralization rate in the last part corresponds to the oxidation of the most stable compounds, indicating the mineralization of RhB is nearly completed.

### 3.8. The proposed mechanism study of RhB removal via simultaneous adsorption and degradation

Fig. 11 illustrates the simultaneous adsorption and degradation of RhB using HMM. As shown in the figure, HMM consists of  $\text{Fe}_3\text{O}_4$  nanoparticles adjacent to each other and forms spherical aggregates via the dissolution and redeposition means (inside-out Ostwald ripening). The mesoporous structure in HMM is intended to increase the accessibility of adsorbing RhB molecules, while the hollow core works as a nanoreactor for the degradation of RhB.

The in-situ adsorption/degradation mechanism using the HMM can be described as follows: All molecules, including RhB in its zwitterionic

Table 4

The computed thermodynamic parameters on the adsorption and degradation of RhB using HMM.

Temperature (K)	Thermodynamic parameters		
	$\Delta G^\circ_{ads}$ (kJ/mol)	$\Delta H^\circ$ (kJ/mol)	$\Delta S^\circ$ (J/mol.K)
303	-0.06	108.7	-357.3
313	-2.05		
323	-7.21		

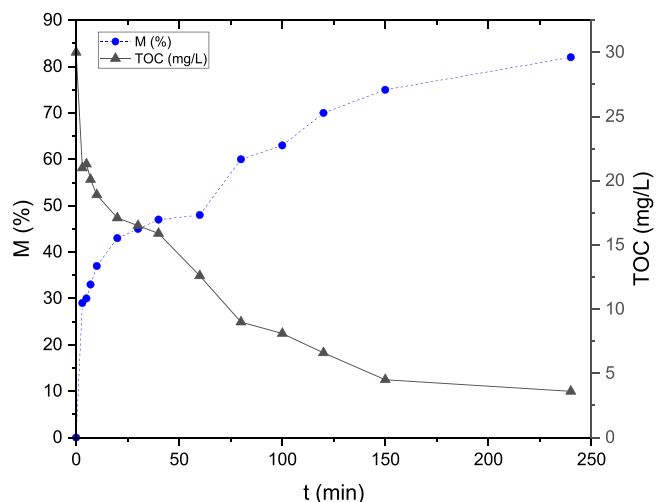


Fig. 10. The mineralization rate (M) and TOC profiles varied with *t*.

form (RhB<sup>-</sup>), water, and H<sub>2</sub>O<sub>2</sub> migrate onto the boundary layer of the catalyst and diffuse through the layer onto the surface of HMM. As the solution pH is set at pH = 6, the binding sites of HMM are available in

the cationic form of FeOH<sup>2+</sup> [63]. The opposite charge between RhB<sup>-</sup> and FeOH<sup>2+</sup> causes some RhB molecules to interact with HMM surface via electrostatic force. Meanwhile, the other RhB molecules diffuse via the mesoporous structure of HMM in which part of RhB molecules is attached to the surface of the pore, and some others move deeper into the hollow core to engage in the Fenton degradation process [64,65]. Initially, H<sub>2</sub>O<sub>2</sub> resonates and undergoes electron delocalization. The negatively charged hydroperoxyl chain then binds with the existing iron (III) ions and releases hydronium ions into the solution. Meanwhile, to stabilize the charge, the electron from the hydroperoxyl chain migrates and reduces the iron (III) ions to iron (II) ions. Subsequently, the hydroperoxyl radicals (•OOH) are formed and released from the surface of HMM.

The degradation continues when other H<sub>2</sub>O<sub>2</sub> molecules undergo the electron excitation in the presence of iron (II) ions on the surface of HMM and destabilize the interaction between the hydroxyl ion and its radical counterpart. This phenomenon oxidizes the iron (II) ions back to iron (III) ions and, at the same time, produces the hydroxyl ions and hydroxyl radicals (•OH). The •OH and •OOH radicals then attack the aromatic chromophore of RhB and promote the reduction of RhB to the simpler components, CO<sub>2</sub> and water, indicated by the bubble formation during the process. Meanwhile, the free hydronium and hydroxyl ions formed from this degradation cycle merge to produce water. Once the

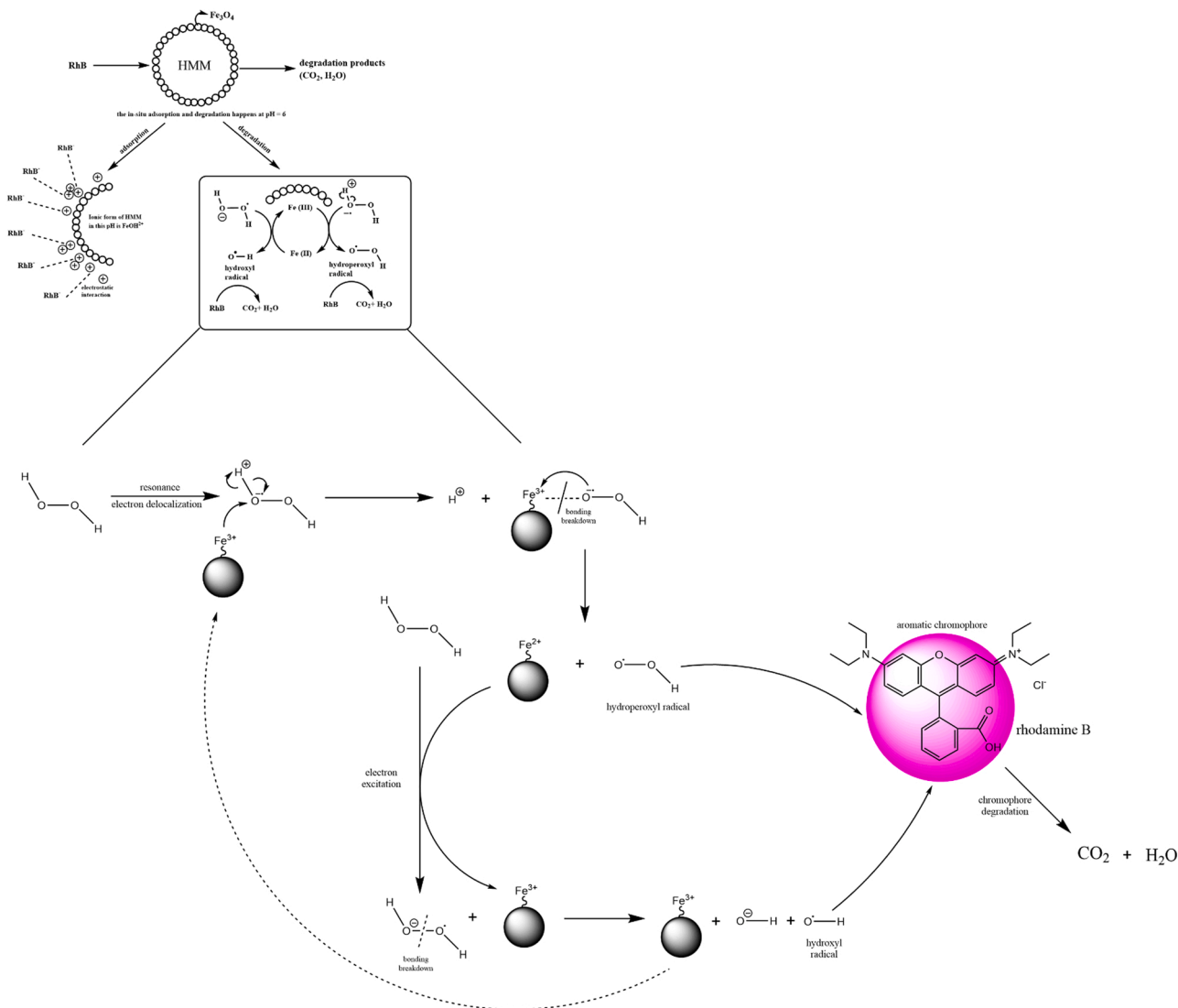


Fig. 11. The proposed mechanism of the simultaneous adsorption and degradation of RhB using HMM.

degradation is completed, all degradation products (CO<sub>2</sub> and water) from the in-situ adsorption/degradation process are subsequently desorbed to the surface of HMM.

#### 4. Conclusion

In this study, hollow mesoporous magnetite (HMM) has been successfully fabricated using the in-situ growth of magnetite on polystyrene surfaces through precipitation and oxidation processes. The obtained HMM spheres have a particle size of 320 – 350 nm and are integrated with a hollow core (with a diameter of 230 nm). The surface area and pore volume of HMM are found at 132.0 m<sup>2</sup>/g and 0.63 cm<sup>3</sup>/g, respectively. In the in-situ adsorption/degradation process of HMM, the highest removal rate (99.7%) is observed at pH = 6, m<sub>c</sub> = 0.8 wt%, T = 50 °C, and time = 240 min, indicating that this adsorbent can be used as an efficient material to adsorb and degrade RhB from aqueous solution. This process follows the pseudo-second-order law and multi-layer mechanism, with film diffusion as the controlling step. Based on the modified Langmuir isotherm, the excellent performance of HMM in removing RhB is also contributed by the Fenton degradation reaction. This magnetic adsorbent will be of immense potential application for removing organic contaminants, particularly synthetic dyes, due to its good performance, simple separation, and ability to perform both adsorption and degradation processes simultaneously.

#### CRedit authorship contribution statement

**Richky Wijaya Abadi:** Conceptualization, Methodology, Software, Visualization, Investigation, Writing – original draft. **Carlos Marcelino Setiawan:** Conceptualization, Methodology, Software, Visualization, Investigation, Writing – original draft. **Shella Permatasari Santoso:** Writing – review & editing, supervision. **Vania Bundjaja:** Software, Investigation. **Artik Elisa Angkawijaya:** Software, Validation. **Yi-Fan Jiang:** Software, Investigation. **Christian Julius Wijaya:** Validation, Supervision. **Suryadi Ismadi:** Resources, Validation, Supervision. **Ery Susiany Retnoningtyas:** Validation, Supervision. **Felycia Edi Soetardedjo:** Resources, Data curation. **Jindrayani Nyoo Putro:** Data curation. **Maria Yuliana:** Conceptualization, Methodology, Software, Visualization, Writing – review & editing, Supervision.

#### Declaration of Competing Interest

The authors declare that they have no known competing financial interests or personal relationships that could have appeared to influence the work reported in this paper.

#### Acknowledgment

The authors thank the National Taiwan University and National Taiwan University of Science and Technology for providing the facilities for material characterizations. This project was supported by Widya Mandala Surabaya Catholic University through research grant no. 3221/WM01/N/2021.

#### References

- [1] L. Zhou, C. Gao, W. Xu, Magnetic dendritic materials for highly efficient adsorption of dyes and drugs, *ACS Appl. Mater. Interfaces* 2 (2010) 1483–1491, <https://doi.org/10.1021/am100114f>.
- [2] M. Isanejad, M. Arzani, H.R. Mahdavi, T. Mohammadi, Novel amine modification of ZIF-8 for improving simultaneous removal of cationic dyes from aqueous solutions using supported liquid membrane, *J. Mol. Liq.* 225 (2017) 800–809, <https://doi.org/10.1016/j.molliq.2016.11.007>.
- [3] S. Merouani, O. Hamdaoui, F. Saoudi, M. Chiha, Sonochemical degradation of Rhodamine B in aqueous phase: effects of additives, *Chem. Eng. J.* 158 (2010) 550–557, <https://doi.org/10.1016/j.cej.2010.01.048>.
- [4] R. Jain, M. Mathur, S. Sikarwar, A. Mittal, Removal of the hazardous dye rhodamine B through photocatalytic and adsorption treatments, *J. Environ. Manag.* 85 (2007) 956–964, <https://doi.org/10.1016/j.jenvman.2006.11.002>.
- [5] Kemenperin, Industri Tekstil dan Pakaian Tumbuh Paling Tinggi, Kementerian Perindustrian Republik Indonesia. (2019). (<https://kemenperin.go.id/artike/1/21191/Industri-Tekstil-dan-Pakaian-Tumbuh-Paling-Tinggi>) (accessed August 11, 2020).
- [6] N. Arbi, Lebih dari 64 Industri Tekstil Diduga Buang Limbah ke Citarum, *CNN Indonesia*. (2018). (<https://www.cnnindonesia.com/ekonomi/20180111214632-92-268281/lebih-dari-64-industri-tekstil-diduga-buang-limbah-ke-citarum>) (accessed August 11, 2020).
- [7] A. Oehmen, D. Vergel, J. Fradinho, M.A.M. Reis, J.G. Crespo, S. Velizarov, Mercury removal from water streams through the ion exchange membrane bioreactor concept, *J. Hazard. Mater.* 264 (2014) 65–70, <https://doi.org/10.1016/j.jhazmat.2013.10.067>.
- [8] T.A. Kurniawan, G.Y.S. Chan, W.H. Lo, S. Babel, Physico-chemical treatment techniques for wastewater laden with heavy metals, *Chem. Eng. J.* 118 (2006) 83–98, <https://doi.org/10.1016/j.cej.2006.01.015>.
- [9] M. Hayasi, M. Karimi, Synthesis of poly(styrene-co-methacrylic acid)-coated magnetite nanoparticles as effective adsorbents for the removal of crystal violet and Rhodamine B: a comparative study, *Polym. Bull.* 74 (2017) 1995–2016, <https://doi.org/10.1007/s00289-016-1816-y>.
- [10] H. Sun, L. Cao, L. Lu, Magnetite/reduced graphene oxide nanocomposites: one step solvothermal synthesis and use as a novel platform for removal of dye pollutants, *Nano Res.* 4 (2011) 550–562, <https://doi.org/10.1007/s12274-011-0111-3>.
- [11] T.M.V. Ngo, T.H.L. Nguyen, X.T. Mai, T.H.N. Pham, T.T.T. Nguyen, T.D. Pham, Adsorptive removal of cationic dyes using hybrid material-based polyelectrolyte modified laterite soil, *J. Environ. Chem. Eng.* 9 (2021), <https://doi.org/10.1016/j.jece.2021.105135>.
- [12] T.D. Pham, T.T. Pham, M.N. Phan, T.M.V. Ngo, V.D. Dang, C.M. Vu, Adsorption characteristics of anionic surfactant onto laterite soil with differently charged surfaces and application for cationic dye removal, *J. Mol. Liq.* 301 (2020), <https://doi.org/10.1016/j.molliq.2020.112456>.
- [13] P. Wang, Q. Shi, Y. Shi, K.K. Clark, G.D. Stucky, A.A. Keller, Magnetic permanently confined micelle arrays for treating hydrophobic organic compound contamination, *J. Am. Chem. Soc.* 131 (2009) 182–188, <https://doi.org/10.1021/ja806556a>.
- [14] T.T. Truong, T.T. Pham, T.T.T. Truong, T.D. Pham, Synthesis, characterization of novel ZnO/CuO nanoparticles, and the applications in photocatalytic performance for rhodamine B dye degradation, *Environ. Sci. Pollut. Res.* 29 (2022) 22576–22588, <https://doi.org/10.1007/s11356-021-17106-0>.
- [15] A.A. Taha, L. Huang, S. Ramakrishna, Y. Liu, MOF [NH<sub>2</sub>-MIL-101(Fe)] as a powerful and reusable Fenton-like catalyst, *J. Water Process Eng.* 33 (2020), <https://doi.org/10.1016/j.jwpe.2019.101004>.
- [16] Y. Zhang, Q. Ruan, Y. Peng, G. Han, H. Huang, C. Zhong, Synthesis of hierarchical-pore metal-organic framework on liter scale for large organic pollutants capture in wastewater, *J. Colloid Interface Sci.* 525 (2018) 39–47, <https://doi.org/10.1016/j.jcis.2018.04.063>.
- [17] X. Gao, M. Zheng, X. Zhao, S. Song, Z. Gao, Ultra-high-capacity adsorption of rhodamine B in a carboxyl-functionalized metal-organic framework via surface adsorption, *J. Chem. Eng. Data* 66 (2021) 669–676, <https://doi.org/10.1021/acs.jced.0c00818>.
- [18] A. Bonilla-Petriciolet, D.I. Mendoza-Castillo, H.E. Reynel-Ávila, Adsorption Processes for Water Treatment and Purification, Springer International Publishing, 2017, <https://doi.org/10.1007/978-3-319-58136-1>.
- [19] Q.A. Pankhurst, J. Connolly, S.K. Jones, J. Dobson, Applications of magnetic nanoparticles in biomedicine, *J. Phys. D Appl. Phys.* 36 (2003) R167–R181.
- [20] M. Kumari, C.U. Pittman, D. Mohan, Heavy metals [chromium (VI) and lead (II)] removal from water using mesoporous magnetite (Fe<sub>3</sub>O<sub>4</sub>) nanospheres, *J. Colloid Interface Sci.* 442 (2015) 120–132, <https://doi.org/10.1016/j.jcis.2014.09.012>.
- [21] Z. Huang, F. Tang, Preparation, structure, and magnetic properties of mesoporous magnetite hollow spheres, *J. Colloid Interface Sci.* 281 (2005) 432–436, <https://doi.org/10.1016/j.jcis.2004.08.121>.
- [22] Y. Jiao, C. Wan, W. Bao, H. Gao, D. Liang, J. Li, Facile hydrothermal synthesis of Fe<sub>3</sub>O<sub>4</sub>@cellulose aerogel nanocomposite and its application in Fenton-like degradation of Rhodamine B, *Carbohydr. Polym.* 189 (2018) 371–378, <https://doi.org/10.1016/j.carbpol.2018.02.028>.
- [23] B. Monárrez-Cordero, P. Amézaga-Madrid, W. Antúnez-Flores, C. Leyva-Porras, P. Pizá-Ruiz, M. Miki-Yoshida, Highly efficient removal of arsenic metal ions with high superficial area hollow magnetite nanoparticles synthesized by AACVD method, *J. Alloy. Compd.* 586 (2014), <https://doi.org/10.1016/j.jallcom.2012.12.073>.
- [24] K. Byrappa, A.K. Subramani, S. Ananda, K.M. Lokanatha Rai, R. Dinesh, M. Yoshimura, Photocatalytic degradation of rhodamine B dye using hydrothermally synthesized ZnO, 2006.
- [25] J.H. Huang, K.L. Huang, S.Q. Liu, A.T. Wang, C. Yan, Adsorption of Rhodamine B and methyl orange on a hypercrosslinked polymeric adsorbent in aqueous solution, *Coll. Surf. A Physicochem. Eng. Asp.* 330 (2008) 55–61, <https://doi.org/10.1016/j.colsurfa.2008.07.050>.
- [26] C.M. Navarathna, N.B. Dewage, A.G. Karunanayake, E.L. Farmer, F. Perez, E. B. Hassan, T.E. Mlsna, C.U. Pittman, Rhodamine B adsorptive removal and photocatalytic degradation on MIL-53-Fe MOF/magnetic magnetite/biochar composites, *J. Inorg. Organomet. Polym. Mater.* 30 (2020) 214–229, <https://doi.org/10.1007/s10904-019-01322-w>.
- [27] V. Quang Tung, B. Minh Quy, V. Quang Túng, B. Minh Quý, Removal of rhodamine b dye from aqueous solution using chitosan-magnetite composite, *TNU Journal of Science and Technology.* 227 (n.d.) 11–18, <https://doi.org/10.34238/tnu-jst.5424>.
- [28] W. Zhang, Y. Lan, M. Ma, S. Chai, Q. Zuo, K.H. Kim, Y. Gao, A novel chitosan–vanadium–titanium–magnetite composite as a superior adsorbent for

- organic dyes in wastewater, *Environ. Int.* 142 (2020), <https://doi.org/10.1016/j.envint.2020.105798>.
- [29] I. Lestari, E. Kurniawan, D.R. Gusti, Yusneli, Magnetite Fe<sub>3</sub>O<sub>4</sub>-activated carbon composite as adsorbent of rhodamine B dye, in: IOP Conference Series: Earth and Environmental Science, Institute of Physics Publishing, 2020. <https://doi.org/10.1088/1755-1315/483/1/012046>.
- [30] Y. Jiao, C. Wan, W. Bao, H. Gao, D. Liang, J. Li, Facile hydrothermal synthesis of Fe<sub>3</sub>O<sub>4</sub>@cellulose aerogel nanocomposite and its application in Fenton-like degradation of Rhodamine B, *Carbohydr. Polym.* 189 (2018) 371–378, <https://doi.org/10.1016/j.carbpol.2018.02.028>.
- [31] Y. Chen, P. Pötschke, J. Pionteck, B. Voit, H. Qi, Fe<sub>3</sub>O<sub>4</sub> nanoparticles grown on cellulose/GO hydrogels as advanced catalytic materials for the heterogeneous fenton-like reaction, *ACS Omega* 4 (2019) 5117–5125, <https://doi.org/10.1021/acsomega.9b00170>.
- [32] S. He, Y. Zhang, J. Ren, B. Wang, Z. Zhang, M. Zhang, Facile synthesis of TiO<sub>2</sub>@MoS<sub>2</sub> hollow microtubes for removal of organic pollutants in water treatment, *Coll. Surf. A Physicochem. Eng. Asp.* 600 (2020), <https://doi.org/10.1016/j.colsurfa.2020.124900>.
- [33] M. Najafi, Y. Yousefi, A.A. Rafati, Synthesis, characterization and adsorption studies of several heavy metal ions on amino-functionalized silica nano hollow sphere and silica gel, *Sep. Purif. Technol.* 85 (2012) 193–205, <https://doi.org/10.1016/j.seppur.2011.10.011>.
- [34] Z. Huang, F. Tang, Preparation, structure, and magnetic properties of polystyrene coated by Fe<sub>3</sub>O<sub>4</sub> nanoparticles, *J. Colloid Interface Sci.* 275 (2004) 142–147, <https://doi.org/10.1016/j.jcis.2003.12.065>.
- [35] E. Shayegan Mehr, M. Sorbiun, A. Ramazani, S. Taghavi Fardood, Plant-mediated synthesis of zinc oxide and copper oxide nanoparticles by using ferulago angulata (schlecht) boiss extract and comparison of their photocatalytic degradation of Rhodamine B (RhB) under visible light irradiation, *J. Mater. Sci. Mater. Electron.* 29 (2018) 1333–1340, <https://doi.org/10.1007/s10854-017-8039-3>.
- [36] D. Maity, J. Ding, J.-M. Xue, Synthesis of magnetite nanoparticles by thermal decomposition: time, temperature, surfactant and solvent effects, *Funct. Mater. Lett.* 1 (2008) 189–193, <https://doi.org/10.1142/S1793604708000381>.
- [37] L. Xu, J. Zhang, J. Ding, T. Liu, G. Shi, X. Li, W. Dang, Y. Cheng, R. Guo, Pore structure and fractal characteristics of different shale lithofacies in the along formation in the western area of the lower yangtze platform, *Minerals* 10 (2020), <https://doi.org/10.3390/min10010072>.
- [38] Ö. Kerkez, Ş.S. Bayazit, Magnetite decorated multi-walled carbon nanotubes for removal of toxic dyes from aqueous solutions, *J. Nanopart. Res.* 16 (2014), <https://doi.org/10.1007/s11051-014-2431-1>.
- [39] M.F. Hou, C.X. Ma, W. De Zhang, X.Y. Tang, Y.N. Fan, H.F. Wan, Removal of rhodamine B using iron-pillared bentonite, *J. Hazard. Mater.* 186 (2011) 1118–1123, <https://doi.org/10.1016/j.jhazmat.2010.11.110>.
- [40] W.S. Tan, A.S.Y. Ting, Alginate-immobilized bentonite clay: adsorption efficacy and reusability for Cu(II) removal from aqueous solution, *Bioresour. Technol.* 160 (2014) 115–118, <https://doi.org/10.1016/j.biortech.2013.12.056>.
- [41] S. Chowdhury, R. Mishra, P. Saha, P. Kushwaha, Adsorption thermodynamics, kinetics and isosteric heat of adsorption of malachite green onto chemically modified rice husk, *Desalination* 265 (2011) 159–168, <https://doi.org/10.1016/j.desal.2010.07.047>.
- [42] R.R. Pawar, P.G. Lalhmunsiam, S.M. Lee Ingole, Use of activated bentonite-alginate composite beads for efficient removal of toxic Cu<sup>2+</sup> and Pb<sup>2+</sup> ions from aquatic environment, *Int. J. Biol. Macromol.* 164 (2020) 3145–3154, <https://doi.org/10.1016/j.ijbiomac.2020.08.130>.
- [43] I. Prasetyo, F. Akbar, A.W. Prabandari, T. Ariyanto, Fenton oxidation using easily recoverable catalyst of magnetite (Fe<sub>3</sub>O<sub>4</sub>) as an efficient approach to treatment of rhodamine B dyeing effluent in traditional fabrics industry, *ASEAN J. Sci. Technol. Dev.* 36 (2019), <https://doi.org/10.29037/ajst.592>.
- [44] P. v Nidheesh, R. Gandhimathi, S. Velmathi, N.S. Sanjini, Magnetite as a heterogeneous electro Fenton catalyst for the removal of Rhodamine B from aqueous solution, *RSC Adv.* 4 (2014) 5698–5708, <https://doi.org/10.1039/c3ra46969g>.
- [45] L. Hu, H. Yuan, L. Zou, F. Chen, X. Hu, Adsorption and visible light-driven photocatalytic degradation of Rhodamine B in aqueous solutions by Ag@AgBr/SBA-15, *Appl. Surf. Sci.* 355 (2015) 706–715, <https://doi.org/10.1016/j.apsusc.2015.04.166>.
- [46] F. Wang, Y. Tang, B. Zhang, B. Chen, Y. Wang, Preparation of novel magnetic hollow mesoporous silica microspheres and their efficient adsorption, *J. Colloid Interface Sci.* 386 (2012) 129–134, <https://doi.org/10.1016/j.jcis.2012.06.088>.
- [47] X. Gao, M. Zheng, X. Zhao, S. Song, Z. Gao, Ultra-high-capacity adsorption of rhodamine B in a carboxyl-functionalized metal-organic framework via surface adsorption, *J. Chem. Eng. Data* 66 (2021) 669–676, <https://doi.org/10.1021/acs.jced.0c00818>.
- [48] L.L. Jiang, H.T. Yu, L.F. Pei, X.G. Hou, The effect of temperatures on the synergistic effect between a magnetic field and functionalized graphene oxide-carbon nanotube composite for Pb<sup>2+</sup> and phenol adsorption, *J. Nanomater.* 2018 (2018), <https://doi.org/10.1155/2018/9167938>.
- [49] P. v Nidheesh, R. Gandhimathi, S. Velmathi, N.S. Sanjini, Magnetite as a heterogeneous electro Fenton catalyst for the removal of Rhodamine B from aqueous solution, *RSC Adv.* 4 (2014) 5698–5708, <https://doi.org/10.1039/c3ra46969g>.
- [50] G.Y. Abate, A.N. Alene, A.T. Habte, Y.A. Addis, Adsorptive removal of basic green dye from aqueous solution using humic acid modified magnetite nanoparticles: kinetics, equilibrium and thermodynamic studies, *J. Polym. Environ.* 29 (2021) 967–984, <https://doi.org/10.1007/s10924-020-01932-3>.
- [51] D. Wan, W. Li, G. Wang, K. Chen, L. Lu, Q. Hu, Adsorption and heterogeneous degradation of rhodamine B on the surface of magnetic bentonite material, *Appl. Surf. Sci.* 349 (2015) 988–996, <https://doi.org/10.1016/j.apsusc.2015.05.004>.
- [52] M. Namdeo, S.K. Bajpai, Investigation of hexavalent chromium uptake by synthetic magnetite nanoparticles, *Electron. J. Environ.* 7 (2008).
- [53] X. Liu, J. Tian, Y. Li, N. Sun, S. Mi, Y. Xie, Z. Chen, Enhanced dyes adsorption from wastewater via Fe<sub>3</sub>O<sub>4</sub> nanoparticles functionalized activated carbon, *J. Hazard. Mater.* 373 (2019) 397–407, <https://doi.org/10.1016/j.jhazmat.2019.03.103>.
- [54] B.C.H. Giles, T.H. Macewan, S.N. Nakhwa, D. Smith, Solution adsorption isotherms, and its use in diagnosis of adsorption mechanisms and in measurement of specific surface areas of solids, *J. Chem. Soc.* (1960) 3973–3993.
- [55] A. Dąbrowski, P. Podkościelny, Z. Hubicki, M. Barczak, Adsorption of phenolic compounds by activated carbon - a critical review, *Chemosphere* 58 (2005) 1049–1070, <https://doi.org/10.1016/j.chemosphere.2004.09.067>.
- [56] C.H. Giles, D. Smith, A. Huitson, A general treatment and classification of the solute adsorption isotherm. I. Theoretical, *J. Colloid Interface Sci.* 47 (1974) 755–765.
- [57] S. Liu, Cooperative adsorption on solid surfaces, *J. Colloid Interface Sci.* 450 (2015) 224–238, <https://doi.org/10.1016/j.jcis.2015.03.013>.
- [58] A.O. Dada, A.P. Olalekan, A.M. Olatunya, Langmuir, Freundlich, Temkin and Dubinin-Radushkevich Isotherms Studies of Equilibrium Sorption of Zn<sup>2+</sup> Unto Phosphoric Acid Modified Rice Husk, *IOSR J. Appl. Chem.* (IOSR-JAC 3 (2012) 38–45, <https://doi.org/10.9790/5736-0313845>.
- [59] M.A. Al-Ghouthi, D.A. Da'ana, Guidelines for the use and interpretation of adsorption isotherm models: a review, *J. Hazard. Mater.* 393 (2020), <https://doi.org/10.1016/j.jhazmat.2020.122383>.
- [60] L. Laysandra, M. Winda Masnora Kartika Sari, F. Edi Soetaredjo, K. Foe, J. Nyoo Putro, A. Kurniawan, Y.-H. Ju, S. Ismadji, Adsorption and photocatalytic performance of bentonite-titanium dioxide composites for methylene blue and rhodamine B decoloration, *Heliyon* 3 (2017) 488, <https://doi.org/10.1016/j.heliyon.2017>.
- [61] O.M. Bankole, O.E. Oyeneyin, S.E. Olaseni, Kinetics and Thermodynamic Studies for Rhodamine B Dye Removal onto Graphene Oxide Nanosheets in Simulated Wastewater and Thermodynamic Kinetics and Thermodynamic Studies for Rhodamine B Dye Removal onto Graphene Oxide Nanosheets in Simulated Wastewater, 2019. <https://doi.org/10.11648/j.ajac.20190701.12>.
- [62] A.H. Mahvi, M. Ghanbarian, S. Nasserli, A. Khairi, Mineralization and decoloration of textile wastewater by TiO<sub>2</sub> nanoparticles, *Desalination* 239 (2009) 309–316, <https://doi.org/10.1016/j.desal.2008.04.002>.
- [63] M. Kumari, C.U. Pittman, D. Mohan, Heavy metals [chromium (VI) and lead (II)] removal from water using mesoporous magnetite (Fe<sub>3</sub>O<sub>4</sub>) nanospheres, *J. Colloid Interface Sci.* 442 (2015) 120–132, <https://doi.org/10.1016/j.jcis.2014.09.012>.
- [64] S. Wang, A Comparative study of Fenton and Fenton-like reaction kinetics in decolorisation of wastewater, *Dyes Pigments* 76 (2008) 714–720, <https://doi.org/10.1016/j.dyepig.2007.01.012>.
- [65] R. Saleh, A. Taufik, Degradation of methylene blue and congo-red dyes using Fenton, photo-Fenton, sono-Fenton, and sonophoto-Fenton methods in the presence of iron(II,III) oxide/zinc oxide/graphene (Fe<sub>3</sub>O<sub>4</sub>/ZnO/graphene) composites, *Sep. Purif. Technol.* 210 (2019) 563–573, <https://doi.org/10.1016/j.seppur.2018.08.030>.